Axial-load response of CFST stub columns with external stainless steel and recycled aggregate concrete: Testing, mechanism analysis and design

Wen-Hao Zhang [a], Rui Wang [a], Hui Zhao [a], Dennis Lam [b], Peng Chen [c]

[a]College of Civil Engineering, Taiyuan University of Technology, Taiyuan 030024, China;

[b]Faculty of Engineering and Informatics, University of Bradford, Bradford BD7 1DP, UK;

[c]Department of Engineering Mechanics, Shijiazhuang Tiedao University, Shijiazhuang 050043, China

---

Abstract

Recycled aggregate concrete filled stainless steel tube (RAC-FSST) is a new type composite member combining the advantage of stainless steel and RAC. In this paper, totally twenty-four RAC-FSST stub columns were tested under axial load, considering the influences of coarse recycled aggregate (CRA) content, steel ratios and compressive strengths of RAC. The obtained results, including the failure patterns, responses of axial load vs. deformation, stress states of external stainless steel tube and inner RAC and confinement effects, were systematically analyzed. Results indicated that all specimens presented good ductility and higher residual strengths after reaching the maximum axial load. The elastic stiffness of RAC-FSSTs obviously declined with the increasing CRA content, while the strain at the ultimate load rose. The inclusion of CRA could advance the occurrence of the confinement and lead to the lower confining pressure. Then, the models predicting the axial response of RAC-FSST stub columns with consideration of confinement action were developed and the current design provisions for the normal CFST and RAC-FST members were employed to evaluate their applicability to RAC-FSSTs. In general, the design rules including EN 1994-1-1:2004, GB 50936-2014 and T/CECS 625-2019 gave a safe and relatively accurate prediction for the ultimate strength of RAC-FSST stub columns.

Keywords: Concrete filled steel tube; Stainless steel; Recycled aggregates; Confinement effect; Stress-strain response; Design provisions

1. Introduction

In recent years, the utilization of stainless steel in engineering structures is becoming increasingly popular, mainly due to its higher ductility, superior corrosion, excellent dynamic, and fire resistances than carbon steel [1-5]. Nevertheless, the initial cost of stainless steel has limited its large-scale application as the structural members. On the other hand, the use of recycled aggregate concrete (RAC) in civil engineering has been extensively explored [6-10]. The crushed demolition concrete is employed as the recycled aggregates for making RAC, which can decrease the consumption of the natural resource and reduce waste pollution. However, RAC presents relatively poorer mechanical properties, higher creep and shrinkage when compared to natural aggregate concrete (NAC). To date, RAC is mainly employed in the non-structural elements, and its application is gradually extending to the structural components. Against above background, an innovative composite member consisting of external stainless steel tube and internal RAC (termed as“RAC-FSST”) was proposed by Yang and Ma [11], aiming at reducing the consumption of the stainless steel and improving the properties of RAC provided by the external tube.

Until now, considerable experimental and numerical investigations have been performed on the mechanical behaviours of RAC filled carbon steel tubes (RAC-FST) [6-8, 12-14] and normal concrete filled stainless steel tube (CFSST) members [15-17]. The axial-loaded response of these two types of members were systematically investigated, including the typical failure mode, load-carrying capacity, elastic stiffness, ductility and the confinement provided by the steel tube. As for the RAC-FST stub columns, Wang et al. [12] and Lyu et al. [14] found that the inclusion of CRA reduces the Young’s modulus of RAC-FSTs and leads to an increment of the strain corresponding to the peak load. In addition, the confinement effects occur earlier as the

CRA replacement increases, mainly owing to the rapid microcrack development of RAC under axial load. For the CFSST stub columns, a series of experiments were conducted on totally 36 specimens (6 specimens by Lam and Gardner [15], 24 by Uy et al. [16] and 6 by Guo et al. [17]). Results indicated that when compared with the normal CFSTs, the combined employment of stainless steel and concrete improves the ductile performance and presents larger residual load-bearing capacities in CFSST stub columns during the late loading phase, mainly attributed to the obvious strain-hardening response of stainless steel.

Compared with the comprehensive researches on RAC-FST and CFSST stub columns, the investigations on the axially-loaded response of RAC-FSSTs are still limited. Table 1 summarizes the detailed experimental parameters of the related studies. Totally 4 circular RAC-FSST stub columns with varying CRA replacement levels (0%, 25%, 50%, 75%) were tested by Yang and Ma [11]. It was found that the modulus of elasticity and the load-carrying capacity of RAC-FSSTs declined with increasing CRA content. When compared to the specimens with NAC, approximate 6.1-18.0% decrease in the axial stiffness was observed in RAC specimens. Following Yang and Ma's study [11], Tam et al. [18] reported experimental results of 4 RAC-FSST stub columns under axial compression. It was concluded that the ultimate strengths of RAC-FSST specimens were more obviously influenced by the CRA content than those of RAC-FST specimens. The decrease in the modulus of elasticity was up to 15% for RAC-FSST stub columns as compared to the counterpart with carbon steel. To date, several key issues on the axially-loaded performance of RAC-FSST stub columns are still not clear, including the confinement effect provided by stainless steel, influence of steel ratio and concrete strength on axial load-strain response, stress states of external steel tube and core RAC, etc. In addition, there is no model to predict the axial load-strain relationships of RAC-

FSST stub columns considering the confinement effect.

Table 1 Experimental parameters of the related studies [11, 18].

Member type	Number of specimens	D (mm)	t (mm)	r (%)	α (%)	$f_{cu,test}$ (MPa)	$\sigma_{0.2}$ (MPa)	Source
RAC-FSST	4	120	1.77	0, 25, 50, 75	6.2	56.9-63.4	286.7	Yang and Ma [11]
	4	169.4	2.86	0, 25, 50, 100	7.1	47.8-52.2	339.6	Tam et al. [18]

Consequently, totally 24 RAC-FSST specimens were tested to investigate axial-load response. The main parameters include CRA replacement level, steel ratio and concrete strength. The failure patterns, axial force-strain responses as well as the circumferential and vertical strains of external stainless steel tube were obtained. Based on these data, the mechanism analysis including the confinement effect and stress states of steel tube and RAC core were further analyzed. In addition, the model equations were developed to simulate the vertical responses of the external steel tube, the core concrete and the whole specimen, in which the influences of stainless steel and CRA content and the restraining action were considered. Finally, the modified equations for the normal CFST and RAC-FST members were evaluated for their applicability to RAC-FSSTs based on the results herein and those from related literatures [11, 15-18]. Five design rules, EN 1994-1-1:2004 [19], AIJ 2008 [20], GB 50936-2014 [21], ANSI/AISC 360-16 [22] and T/CECS 625-2019 [23], were considered in this work.

2. Test programs

2.1. Design of specimen

A total of 24 stub columns were prepared in this study, in which three CRA replacement levels r, two steel ratios α (=A_s/A_c, A_c and A_s represent the areas of core concrete and steel tube, respectively) and two water/cement ratios (w/c) of RAC were designed. The S30408 seamless stainless steel tube was chosen in the test. The height-diameter ratio was maintained at 3 to ensure that the samples are not be failed by flexural buckling. Details of the specimens are given in Table 2. The following designation system was

Table 2 Details of specimens and corresponding test results.

Group	Specimen labels	$D \times t \times L$ (mm)	r (%)	α (%)	$f_{cu,test}$ (MPa)	N_u (kN)		EA ($\times 10^5$kN)		ε_u ($\mu\varepsilon$)	
						Tested	Average	Tested	Average	Tested	Average
1	L-219-0-1	219 × 3.9 × 620	0	7.5	44.5	2271	2354	13.38	14.88	9591	9268
	L-219-0-2	219 × 3.9 × 620	0	7.5	44.5	2459		14.51		9302	
	L-219-0-3	219 × 3.9 × 620	0	7.5	44.5	2331		16.76		8912	
2	L-219-50-1	219 × 3.9 × 620	50	7.5	41.4	2242	2274	13.12	12.21	11419	10963
	L-219-50-2*	219 × 3.9 × 620	50	7.5	41.4	2304*		18.15*		7011*	
	L-219-50-3	219 × 3.9 × 620	50	7.5	41.4	2306		11.30		10507	
3	L-219-100-1	219 × 3.9 × 620	100	7.5	42.3	2254	2247	11.72	11.85	12762	12250
	L-219-100-2	219 × 3.9 × 620	100	7.5	42.3	2270		12.35		11349	
	L-219-100-3	219 × 3.9 × 620	100	7.5	42.3	2218		11.48		12639	
4	L-114-0-1	114 × 4.2 × 350	0	16.5	44.5	1082	1099	4.31	4.31	10000	10000
	L-114-0-2	114 × 4.2 × 350	0	16.5	44.5	1099		3.66		10000	
	L-114-0-3	114 × 4.2 × 350	0	16.5	44.5	1116		4.97		10000	
5	L-114-50-1	114 × 4.2 × 350	50	16.5	41.4	1053	1016	4.35	4.01	10000	10000
	L-114-50-2	114 × 4.2 × 350	50	16.5	41.4	956		3.80		10000	
	L-114-50-3	114 × 4.2 × 350	50	16.5	41.4	1040		3.88		10000	
6	L-114-100-1	114 × 4.2 × 350	100	16.5	42.3	1016	1010	4.20	3.86	10000	10000
	L-114-100-2	114 × 4.2 × 350	100	16.5	42.3	1023		3.46		10000	
	L-114-100-3	114 × 4.2 × 350	100	16.5	42.3	990		3.93		10000	
7	H-114-0-1	114 × 4.2 × 350	0	16.5	65.8	1318	1317	4.86	4.76	7269	6673
	H-114-0-2	114 × 4.2 × 350	0	16.5	65.8	1317		4.65		6077	
8	H-114-50-1	114 × 4.2 × 350	50	16.5	57.3	1171	1173	4.40	4.33	10000	10000
	H-114-50-2	114 × 4.2 × 350	50	16.5	57.3	1174		4.26		10000	
9	H-114-100-1	114 × 4.2 × 350	100	16.5	52.1	1074	1083	3.91	4.00	10000	10000
	H-114-100-2	114 × 4.2 × 350	100	16.5	52.1	1091		4.10		10000	

* The test result of L-219-50-2 was not considered owing to that the specimen was not concentrically loaded.

adopted, where the first letters 'L' and 'H' denote low and high-strength concrete corresponding to w/c ratio of 0.49 and 0.35, respectively; the first numbers '114' and '219' represent the external diameter of steel tube, respectively; the second numbers '0', '50' and '100' stand for CRA replacement ratios, respectively; the last numbers '1', '2' and '3' are used to identify the repeated specimens in one group.

2.2. Materials and specimen preparations

Totally six tensile coupons were cut from two sizes of steel tubes in longitudinal direction. The mechanical properties were measured in accordance with EN ISO 6892-1 [24] with the instruments including strain gauges and an extensometer. Figs. 1(a) and 1(b) present the tensile coupon test-setup and the engineering stress-strain curves of stainless steel, respectively. As shown in tensile curves, the stainless steel presents rounded stress-strain responses and obvious strain-hardening behaviour. This could result in an enhanced ductility in the stainless steel composite members. Table 3 gives the mean mechanical properties including the Young's modulus (E_0), nominal yield and ultimate strengths ($\sigma_{0.2}$ and σ_u), elongation after fracture ($\Delta L/L_0$), Poisson's ratio (μ_s) and strain-hardening exponent (n). The 0.2% proof stress ($\sigma_{0.2}$) is employed to define the nominal yield stress, as suggested by Han et al. [3].

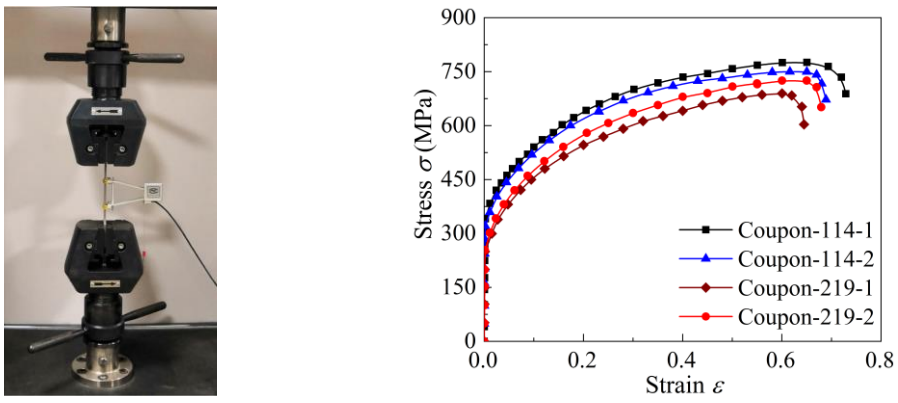

(a) Tensile coupon test-setup (b) Stress-strain response

Fig.1. Tensile test and stress-strain curves of S30408 stainless steel.

Table 3 Mechanical properties of stainless steel.

D (mm)	t (mm)	$\sigma_{0.2}$ (MPa)	σ_u (MPa)	E_0 (GPa)	$\Delta L/L_0$ (%)	μ_s	n
114	4.2	346.1	769.3	199.5	70.0	0.305	5.9
219	3.9	269.3	710.1	203.5	74.3	0.271	9.1

The CRAs were obtained from a demolition frame building built in 1980 and the cubic concrete strength of the column members was estimated to be about 45 MPa through drilled cores. A 2-phase crushing process was adopted to produce CRAs. A mechanical excavator was adopted at the demolition site during the first phase, and then the second-phase crushing was performed by a jaw crusher in the laboratory. The photos and properties of CNAs and CRAs are given in Fig. 2 and Table 4, respectively. As shown, the water absorption of CRAs is greater than that of CNAs, mainly owing to the attached mortar. Therefore, in order to achieve a reasonable concrete workability and mechanical properties, the CRAs were completely soaked in water for around 24 h and then dried to a saturated-surface-dry (SSD) state [25, 26]. For each concrete mix, 3 cubic and 3 prism samples with dimensions of 150 ×150 × 150 mm and 150 ×150 × 300 mm were fabricated to determine the compressive strengths ($f_{cu,test}$) and elastic moduli ($E_{c,test}$) at the time of test day, respectively. Table 5 presents the mixture proportions and the compressive properties of six types of concrete.

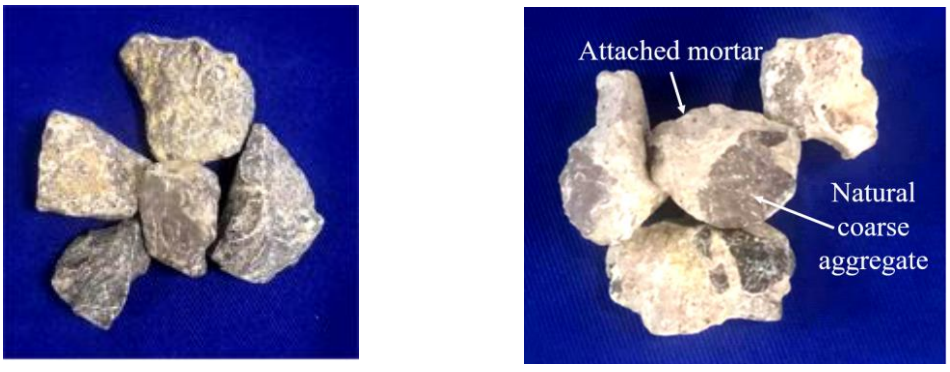

(a) CNAs (b)CRAs

Fig.2. Coarse aggregates.

Table 4 Basic properties of aggregates.

Type	Grading (mm)	Apparent density (kg/m^3)	Water absorption (%)	Index of crushing (%)	Residual mortar (%)
CRA	5.0-25.0	2670	4.80	13.0	38.6
CNA	5.0-25.0	2781	0.49	3.7	—
FNA	0-5.0	2658	3.45	—	—

Table 5 Mixture proportions and the mechanical properties of concrete.

Effective w/c ratio	r (%)	Water (kg/m^3)	Cement (kg/m^3)	Sand (kg/m^3)	CNA (kg/m^3)	CRA (kg/m^3)	SP[a] (kg/m^3)	$f_{cu,test}$ (MPa)	$E_{c,test}$ (MPa)
0.49	0	215	439	624	1108.9	0.0	1.10	44.5	31239
	50	215	439	616	547.3	547.3	1.10	41.4	25736
	100	215	439	608	0.0	1080.7	1.10	42.3	24128
0.35	0	215	614	554	984.0	0.0	3.07	65.8	35743
	50	215	614	535	475.3	475.3	3.07	57.3	29631
	100	215	614	517	0.0	919.5	3.07	52.1	24660

[a] SP is the superplasticizer.

All employed tubes were cut from the seamless steel tube, see Fig. 3(a). To ensure that the infilled concrete and outer tube work together under axial load, the RAC-FSST specimens were prepared as follows: Firstly, a 20 mm thick steel plate was welded to the bottom end of the tube before concrete pouring. Then the concrete was casted slightly higher than the tube and after 28 d curing, the top of the concrete was ground to achieve a smooth and flat surface (Fig. 3(b)). Finally, the other steel plate was welded. All specimens before testing are presented in Fig. 3(c).

(a) Bench saw for cutting

(b) Specimens after grinding

(c) Photo of all RAC-FSST specimens

Fig.3. Specimen preparations.

2.3. Experimental setup and measurement

Experiments were performed using a 5000 kN hydraulic compression machine. Fig. 4 presents the test scene and schematic view of the whole loading set-up and instrumentation arrangements. The axial deformations of the specimens were measured using 4 LVDTs. Eight strain gauges were used to measure the vertical and circumferential strains at the 1/2 height of the columns.

Before compression, the specimen position was adjusted to ensure that the force was concentrically applied to the specimen. A preloading stage was conducted within the range of 30% of the estimated load-bearing capacity. During the initial loading phase, the specimens were loaded with a speed of 1 kN/s and the load interval was set as 100 kN. When the load reached 70% of the estimated strength, the displacement-control loading with a rate of 1 mm/min was employed until failure. Due to the greater ductility of CFSTs with external stainless steel tube [27, 28], the load may increase continuously during the late loading phase. For comparison, the load was terminated when the axial shortening reached 20 mm and 40 mm for specimens with diameters of 114 mm and 219 mm, respectively.

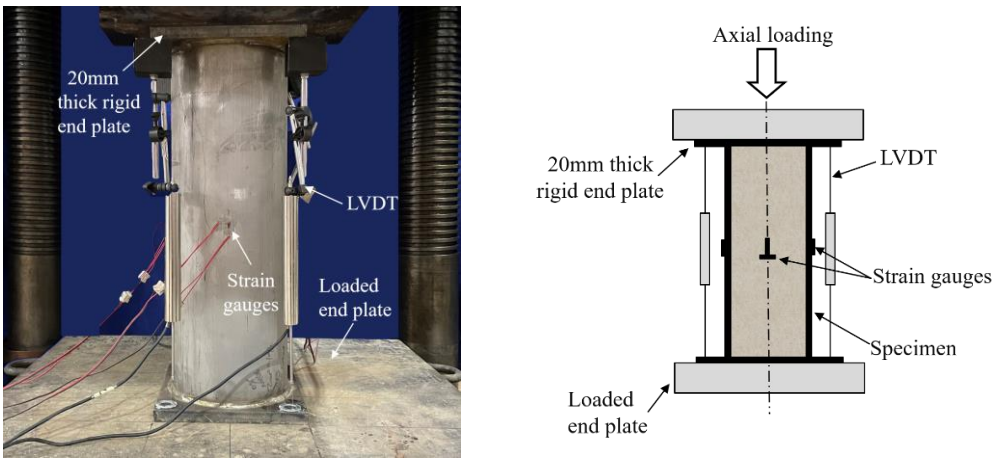

(a) Test scene (b) Schematic view

Fig.4. Loading set-up and instrumentation arrangements.

3. Experimental results and analysis

3.1. Failure pattern

Fig. 5 presents the typical failure patterns of RAC-FSSTs, which can be categorized into 2 types. The specimens with steel ratio of 7.5% showed typical shear failure and the outward buckling occurred at the position of one end and the mid-height. The angles between failure and horizontal planes were around 55°-60°. For specimens with higher steel ratio of 16.5%, the drum-like deformation exhibited at the mid-height and ends of specimens.

(a) α=7.5% (b) α=16.5%

Fig.5. Typical failure patterns of RAC-FSSTs.

After testing, the external tube was removed and the damage of infilled RAC was observed. Fig. 6 gives the photos and schematic diagram of concrete damage for the representative Samples L-219-0-1 and H-114-100-1. As shown, the crushed concrete was observed at the position that the occurrence of outward buckling. Several narrow cracks were located at around 1/3 height of the specimens. More microcracks were observed for Sample H-114-100-1 with higher steel ratio, which illustrated that stronger confinement effect could effectively restrained occurrence of penetrating cracks. In general, the inner concrete remained good integrity. Similar failure patterns were found among specimens with different CRA content. In addition, no scratch was observed at

the internal surface of the tube, indicating that the outer steel tube and inner concrete worked together under the axial load.

(a) L-219-0-1 (b) H-114-100-1

Fig. 6. Core concrete damage.

3.2. Axial load vs. strain responses

The axial load vs. strain responses of all specimens are illustrated in Fig. 7. As presented, the usage of RAC had an insignificant effect on the development trends of the stress-strain curves. In general, the responses of N-ε_v can be divided into 2 types, as shown in Fig. 8, which is mainly related to the confinement effect. For the specimens with steel ratio α of 7.5%, the type A curves were presented, mainly including the elastic (0-1), elastic-plastic (1-2), declining (2-3) and nearly horizontal (3-4) portions. As the value of α increases to 16.5%, the N-ε_v curves exhibit an obvious strain-hardening behaviour (2′-3′) after an elastic-plastic phase (type B). These two types of curves indicate that the external stainless steel tube could provide a good confinement on the core concrete during the late loading phase.

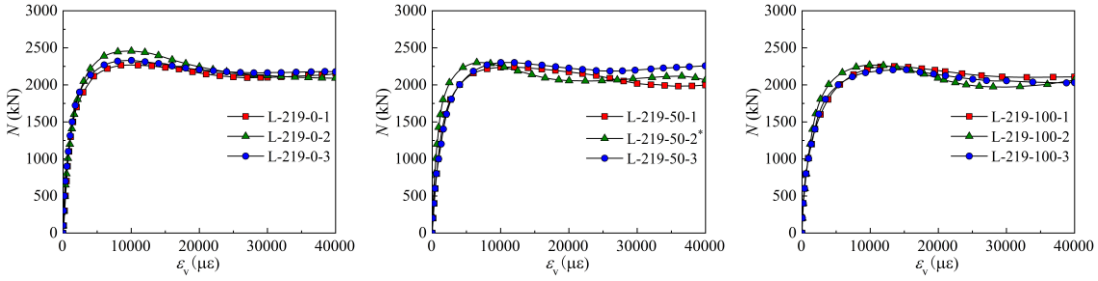

(a) L-219-0 (b) L-219-50 (c) L-219-100

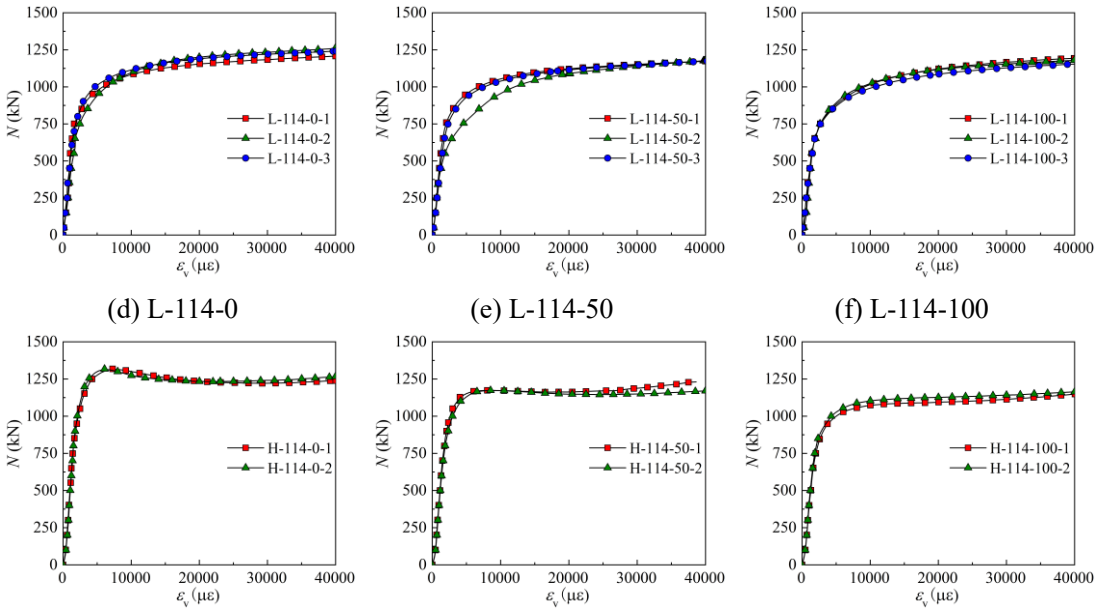

(d) L-114-0 (e) L-114-50 (f) L-114-100

(g) H-114-0 (h) H-114-50 (i) H-114-100

Fig.7. Axial load (N) vs. vertical strain (ε_v) curves of RAC-FSSTs.

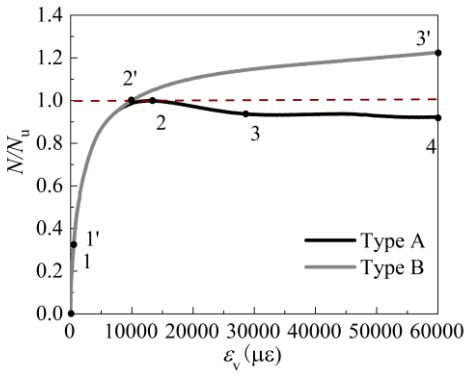

Fig.8. Typical N-ε_v curves of RAC-FSSTs under axial load.

3.3. Influence of CRA replacement

As distinguished from the similar development trends of N-ε_v curves, the elastic stiffness (EA), ultimate strength (N_u) and corresponding strain (ε_u) are affected by CRA content in different degree. For curves without a declining portion, the N_u is taken as the load corresponding to 1% axial strain for comparison, as suggested by Uy et al. [16] and Wang et al. [29]. The secant modulus at 40% of N_u is defined as the EA.

Figs. 9(a)-(c) illustrate the variations of the N_u, ε_u and EA along with the CRA replacement level, respectively. The error bars denoting the standard deviation are also given in the figures to reflect the data scatter. As presented in Fig. 9(a), the values of N_u

were moderately affected by the CRA replacements. The difference of 3.4% and 4.5% were observed for the N_u when the replacement level rose from 0% to 50% and 100% for Samples L-219. Similar moderate influence of CRA content on the N_u also has also been found in other types of CFST members [12, 30, 31]. For the EA and ε_u, the incorporation of CRA obviously affected these two indexes. As the CRA replacement rose, the value of EA declined, while the ε_u increased. For example, when the CRA replacement rose from 0% to 100%, the values of EA and ε_u for Samples L-219 decreased by 20.4% and increased by 32.2%, respectively. Test results indicated that the incorporation of CRA resulted in the lower axial stiffness and larger strain at N_u, which was mainly due to the lower stiffness of the CRA induced by attached old mortar. Generally, the relatively standard deviations are mainly lower than 10%, indicating the dispersion of test results is small.

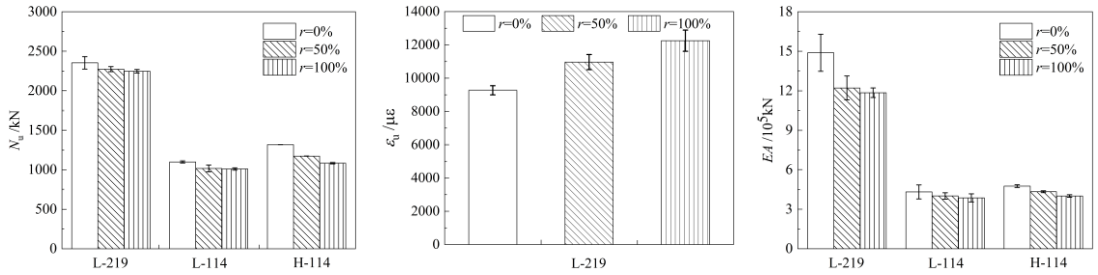

(a) Ultimate strength (b) Strain at maximum load (c) Elastic stiffness

Fig.9. Influence of CRA replacement levels.

3.4. Confinement analysis

3.4.1. Onset of confinement

To clarify the initiation of the confinement under axial compression, the evolutions of measured circumferential strain ($\varepsilon_{s,c}$)/vertical strain ($\varepsilon_{s,v}$) of the stainless steel tube for representative samples L-219, L-114 and H-114 are illustrated in Fig. 10. As shown, the $\varepsilon_{s,c}/\varepsilon_{s,v}$ rose with an increment of the load. During the initial load phase, the values of $\varepsilon_{s,c}/\varepsilon_{s,v}$ were basically in the range of 0.2-0.3, which were near to the μ_s, demonstrating

that the steel tube was under uniaxial compression condition and the confinement did not begin to work. As the load increased continuously, the values of $\varepsilon_{s,c}/\varepsilon_{s,v}$ kept rising, mainly owing to the development of cracks in core concrete. When the $\varepsilon_{s,c}/\varepsilon_{s,v}$ exceeded μ_s, the confinement effect started. In this work, the force corresponding to the onset of confinement effect is defined as N_{ce}. Fig. 11 presents the effects of CRA replacement level on N_{ce}/N_u. As shown, the larger incorporation of CRAs, the earlier confinement effect produces. Taking Samples L-219 for example, the mean values of N_{ce}/N_u declined by 6.3% and 17.0% when r ranged from 0% to 50% and 100%, respectively. The earlier emergence of confining effect was mainly attributed the faster microcrack development of RAC induced by the attached mortar on the CRAs. Similar trends were also observed in Samples L-114 and H-114 with higher α and concrete strength, see Figs. 10(b) and 10(c).

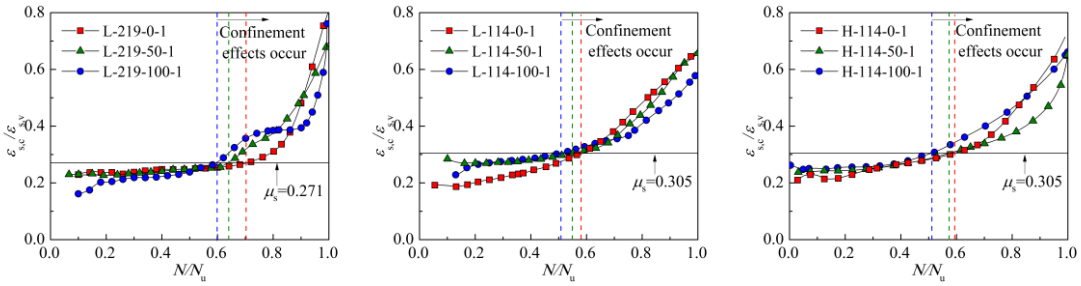

(a) L-219 (b) L-114 (c) H-114

Fig.10. Evolutions of $\varepsilon_{s,c}/\varepsilon_{s,v}$ for different types of specimens.

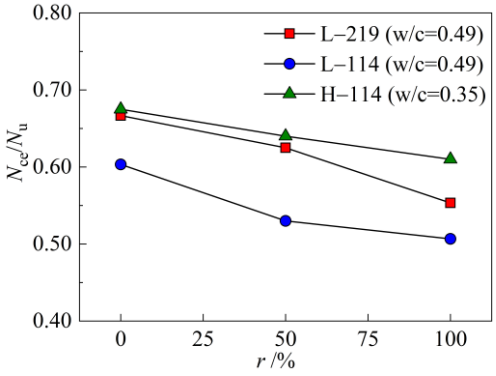

Fig.11. Effects of CRA content on N_{ce}/N_u.

3.4.2. Stress analysis

Under axial compression, the plane stress assumption for steel tube by considering the vertical and circumferential stresses ($\sigma_{s,v}$ and $\sigma_{s,c}$) is valid, mainly due to the thin-walled steel tube resulting in a low radial stress ($\sigma_{s,r}$) [32, 33]. Therefore, a stress analysis method proposed by Wang et al. [34, 35] and measured tube strains are employed to analyze the stress states of steel tube including the vertical, circumferential and equivalent stresses ($\sigma_{s,v}$, $\sigma_{s,c}$, and σ_s). Detailed equations are given in Appendix A, in which the stress-strain relationship of stainless steel under uniaxial load proposed by Rasmussen [36] is adopted and the incremental theory is used to calculate the stress of the steel tube under biaxial stress state. Finally, the axial load-bearing capacity of external stainless steel tube N_s and the vertical stress of core concrete $\sigma_{c,v}$ can be calculated using Eqs. (1) and (2), respectively.

$$N_s=\sigma_{s,v}A_s \tag{1}$$

$$\sigma_{c,v}=(N-N_s)/A_c \tag{2}$$

Fig. 12 presents the developments of $\sigma_{s,v}$, $\sigma_{s,c}$, σ and $\sigma_{c,v}$ along with the vertical strain ε_v for typical Sample L-219-100-1. For the response of $\sigma_{s,v}$-ε_v, three distinct stages including the elastic (O-A), elastic-plastic (A-B) and plastic (B-C) portions can be observed. During O-A stage, the $\sigma_{s,v}$ was close to σ_s, and the positive value of $\sigma_{s,c}$ indicated that the circumferential compressive stress existed in the steel tube, mainly due to the existence of bond strength. In the following A-B stage, the value of $\sigma_{s,c}$ gradually changed from compression (positive) to tension (negative), which demonstrated that the confinement effects generate and develop during this phase. At point B (yield point for steel tube), because of the existence of $\sigma_{s,c}$, the $\sigma_{s,v}$ was around 1.1% lower than the equivalent stress σ_s. During B-C stage, the values of $\sigma_{s,c}$ and $\sigma_{c,v}$ continuously grew, indicating that confining effects became obvious and the stress of

core concrete was further strengthened. Under axial strain of 0.01, the value of $\sigma_{c,v}$ was 48.8 % higher than corresponding prismatic compressive strength.

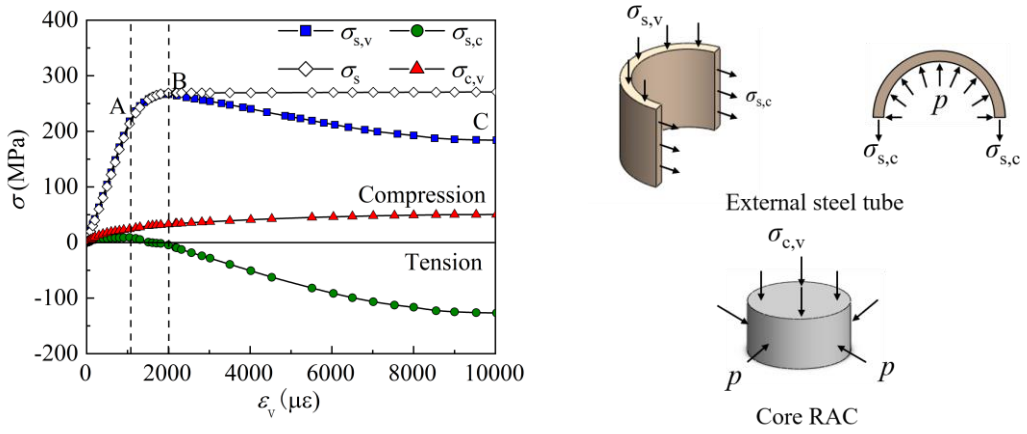

Fig.12. Stress states of stainless steel tube and core RAC for Sample L-219-100-1.

3.4.3. Confining stress from stainless steel tube

For CFST columns, the confining stress p from external steel tube can be calculated using Eq. (3) to quantitatively assess the confinement effect [37-39].

$$p=\frac{2t}{D-2t}\sigma_{s,c} \tag{3}$$

Fig. 13(a) presents the developments of p with vertical strain ε_v for Samples L-219 having different CRA content. As presented, the values of p decreased as the CRA replacement level increases. For instance, the values of p at ε_v=10000με for r=100% and r=50% were 31.8% and 18.5% lower than that of sample with r=0%, respectively. This indicated that the incorporation of CRA would result in a declining confinement in RAC-FSSTs. In Figs. 13(b) and 13(c), higher p was observed in the samples with higher steel ratio and lower concrete strength. The generation of p was postponed in Sample H-114-100-1 as compared to that of Sample L-114-100-3, which was mainly caused by less lateral expansion of the high strength concrete.

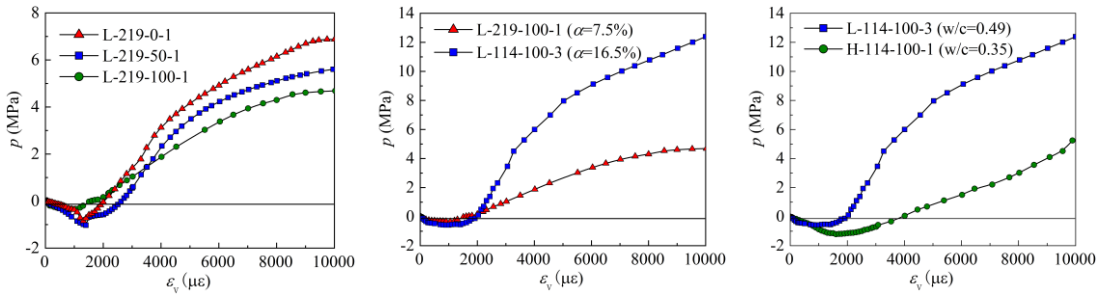

(a) Effect of r (b) Effect of α (c) Effect of w/c

Fig. 13. Developments of p for samples with different parameters.

4. Vertical stress-strain relationships of external steel tube and core RAC

4.1. External steel tube

Similar development trends were observed between the vertical stresses ($\sigma_{s,v}$) of external stainless and carbon steel tubes, by comparing the curves presented in Fig. 12. and those obtained by Wang et al. [12, 33]. Therefore, the model of the $\sigma_{s,v}$-ε_v relationship for RAC-FSTs considering the confinement effect (Eqs. (4)-(6)) was modified to make it suitable for RAC-FSSTs. The influences of CRA replacement on the peak vertical stresses $\sigma_{su,r}$ and corresponding strains $\varepsilon_{su,r}$ of steel tube were incorporated in the model. In the tests reported herein, the $\sigma_{su,r}$ of stainless steel tube gradually increased with the rising CRA replacement, while the $\varepsilon_{su,r}$ kept declining, as shown in Fig. 14. To account for such influence, the equations for the $\sigma_{su,r}$ and $\varepsilon_{su,r}$ were modified according to the test data, as presented in Eqs. (7) and (8).

$$\sigma_{s,v}=\begin{cases} E_0\varepsilon_v & \varepsilon_v\le\varepsilon_{sp} \\ a\varepsilon_v^2+3E_0\varepsilon_v-\sigma_{sp} & \varepsilon_{sp}<\varepsilon_v\le\varepsilon_{su,r} \\ \sigma_{su,r}+b\sigma_{0.2}\ln(\varepsilon_v/\varepsilon_{su,r}) & \varepsilon_v\ge\varepsilon_{su,r} \end{cases} \tag{4}$$

$$a=-E_0/\varepsilon_{sp} \tag{5}$$

$$b=-0.18(\alpha f_{cu}{\sigma_{0.2}}^{0.1})^{-0.3} \tag{6}$$

$$\sigma_{su,r}=(1+0.07r)k\sigma_{0.2} \tag{7}$$

$$\varepsilon_{su,r}=(1-0.05r)\varepsilon_{su} \tag{8}$$

in which σ_{sp} and ε_{sp} are the proportional vertical stresses and corresponding strains of steel tube, respectively, k is the factor related to the steel ratio, concrete strength and

yield-strength of steel tube, as explained in literatures [12, 13]. For stainless steel, the yield strength is taken as the 0.2% proof strength.

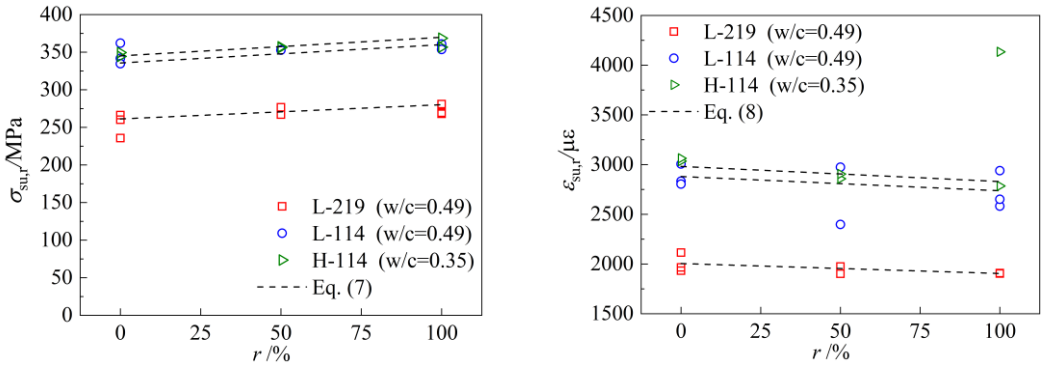

(a) $\sigma_{su,r}$ (b) $\varepsilon_{su,r}$

Fig.14. Influences of CRA content on $\sigma_{su,r}$ and $\varepsilon_{su,r}$.

4.2. Core RAC

The confined concrete model proposed by Mander et al. [40] was used to predict the vertical stress-strain relationship of infilled concrete in RAC-FSSTs, see Eqs. (9) and (10). This model can reasonably predict the vertical stress of core RAC in RAC-FSTs, by considering the influences of CRA replacement level on the compressive behaviours of RAC [12, 13]. Eqs. (11) and (12) present the development of the elastic modulus ($E_{c,r}$) and the strain at peak stress ($\varepsilon_{cc,r}$) of RAC with the CRA replacement, as proposed by Belén et al. [41].

$$\sigma_{c,v}=\frac{(\varepsilon_{c,v}/\varepsilon_{cc,r})\beta}{\beta-1+(\varepsilon_{c,v}/\varepsilon_{cc,r})^{\beta}}f'_{cc,r} \tag{9}$$

$$\beta=\frac{E_{c,r}}{E_{c,r}-f'_{cc,r}/\varepsilon_{cc,r}} \tag{10}$$

$$E_{c,r}=(1-0.2r)E_c \tag{11}$$

$$\varepsilon_{cc,r}=(1+0.21r)\varepsilon_{cc} \tag{12}$$

$$f'_{cc,r}=f_{c,r}+6.7p^{0.83} \tag{13}$$

$$\sigma_{s,c}=\begin{cases} 0 & \varepsilon_v \le \varepsilon_{sp} \\ \left[-9\left(\dfrac{\varepsilon_v}{\varepsilon_{su,r}}\right)^2+18\left(\dfrac{\varepsilon_v}{\varepsilon_{su,r}}\right)-8\right]\sigma_{scu,r} & \varepsilon_{sp} \le \varepsilon_v \le \varepsilon_{su,r} \\ \dfrac{\sigma_{s,v}}{2}-\sqrt{\sigma_{0.2}^2-0.75\sigma_{s,v}^2} & \varepsilon_v \ge \varepsilon_{su,r} \end{cases} \quad (14)$$

$$\sigma_{scu,r}=\frac{\sigma_{su,r}}{2}-\sqrt{\sigma_{0.2}^2-0.75\sigma_{su,r}^2} \quad (15)$$

where $f_{cc,r}^{'}$ represents the maximum stress of confined concrete, calculated using Eq. (13) developed by Marques et al. [42]; $f_{c,r}$ is prismatic compressive strength of RAC; p is confining pressure, as calculated by Eqs. (3), (14) and (15), in which $\sigma_{scu,r}$ represents the circumferential stress of steel tube corresponding to $\varepsilon_{su,r}$.

4.3. Verification of model

To verify the accuracy of the predicted model, the tested stress-strain curves of external stainless steel and core RAC presented herein are compared with the predicted results, as presented in Figs. B.1 and B.2. In addition, the developed models are also employed to simulate the vertical responses of RAC-FSST and CFSST members, respectively from this work and literatures [11, 17, 18]. The comparison results are illustrated in Fig. B.3. Overall, the developed models can reasonably predict the developments of the stress/load responses of these members, including the elastic, elastic-plastic and strain-hardening or strain-softening portions. The average value for the predicted-to-test ultimate strength is 1.044 with standard deviation of 0.096. Some discrepancies are observed between the predict and measured curves, especially during the late load phase, which is mainly owing to the material property deviation between the test and model prediction.

5. Comparisons with existing design methods

Given that no codes are available for the design of RAC-FSST members, the current design methods for normal CFST and RAC-FST members are tentatively used to assess

their applicability in RAC-FSSTs. Test database of 68 specimens from this work and other literatures was employed to compare, including 32 RAC-FSST specimens and remained 36 CFSST specimens. Five design codes were considered, including EN 1994-1-1:2004 [19], AIJ 2008 [20], GB 50936-2014 [21], ANSI/AISC 360-16 [22] and T/CECS 625-2019 [23]. To ensure a direct comparison between the code calculations and experimental data, the material property indexes were taken as the test values and corresponding partial safety factors were set as unity.

Fig. 15 presents the comparison results for each design code, and the mean values and corresponding standard deviations of calculated load N_{uc}/tested load N_{ue} are also given. As shown, all 5 codes gave conservative predictions for the axial load-bearing capacities of RAC-FSSTs. The EC4 [19], GB [21] and T/CECS [23] gave relatively reasonable predictions, respectively 10.0%, 15.2% and 17.8% underestimation as compared to the test results. Owing to a conservative estimation of confinement effect, more lower predictions were observed for AIJ [20] and AISC [22] expressions, respectively 22.2% and 26.6% underestimation.

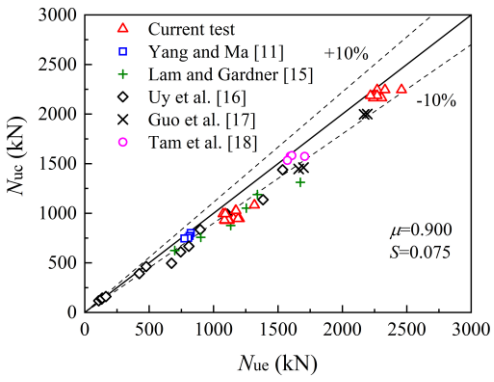

(a) EN 1994-1-1 [19]

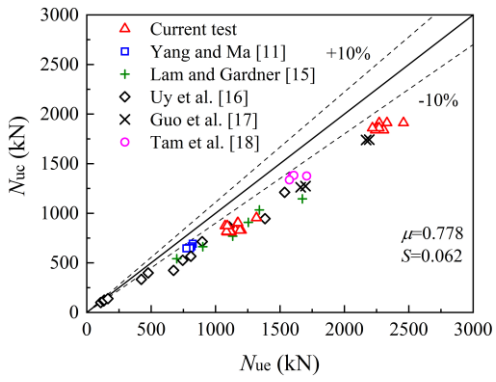

(b) AIJ 2008 [20]

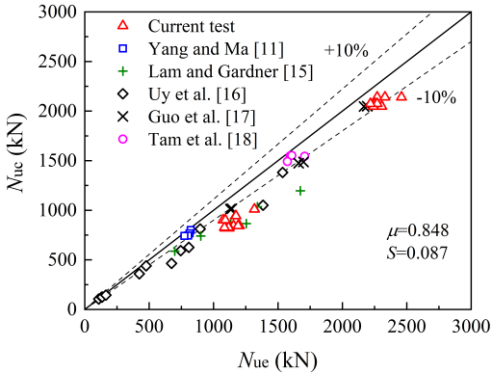

(c) GB 50936-2014 [21]

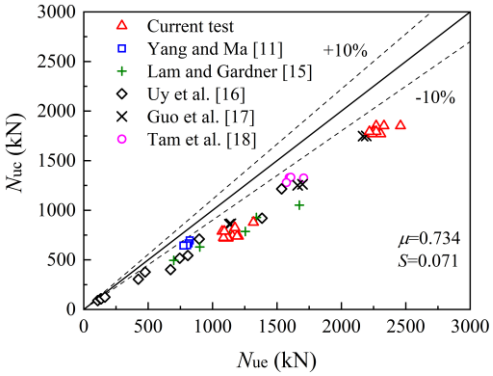

(d) ANSI/AISC 360-16 [22]

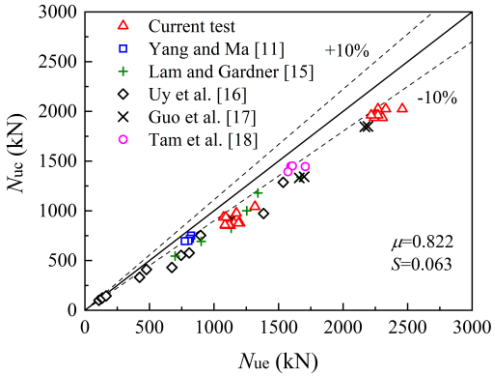

(e) T/CECS 625-2019 [23]

Fig.15. Evaluations of N_u to RAC-FSSTs by available design codes.

6. Conclusions

This work investigated the axial-load responses of RAC-FSST stub columns. The test results and the mechanism of confinement from stainless steel tube to infilled RAC were analyzed in detail. In addition, model equations were developed to simulate the axial responses of RAC-FSST specimens and each component part. Finally, the applicability of the available design codes for normal CFSTs and RAC-FSTs was evaluated. Within the scope of current research, the main conclusions are drawn:

(1) Similar failure modes were observed among specimens with varying CRA replacement levels. Specimens with steel ratio of 7.5% mainly presented with the shear failure and the localized outward buckling, while the drum-like failure pattern was observed at the mid-height and ends of specimens having steel ratio of 16.5%.

(2) There were 2 types of axial force-strain curves for RAC-FSST specimens with

different steel ratios, respectively showing as the strain-softening and strain-hardening responses during the late loading phase. All specimens showed higher residual load-carrying capacity and good ductility. The inclusion of CRA resulted in the reduction of the elastic stiffness and an increase of the strain at the peak load, mainly owning to the lower stiffness of RAC.

(3) Due to the faster microcrack development of RAC caused by the old mortar, the confinement effect occurred earlier as the CRA content increased. Samples with lower CRA content and concrete strength or higher steel ratio presented larger confining pressure p.

(4) A simplified model for the vertical responses of RAC-FSSTs and each component part (outer stainless steel tube and core RAC) under axial compression was developed, with the consideration of the influence of material property and confinement effect. Generally, the suggested model could reasonably predict the load/stress-strain developments of the CFSTs with external stainless steel tube.

(5) Design specifications for normal CFST and RAC-FST members employed in this paper generally underestimated the axial load-bearing capacities of RAC-FSST specimens by comparing the results presented herein and those from the related literatures, in which EC4, GB 50936-2014 and T/CECS 625-2019 provided relatively accurate predictions.

Acknowledgements

This work was supported by the National Natural Science Foundation (No. 52108162).

Appendix A. Stress-strain relationship of stainless steel tube in the analysis of confinement effect

A.1. Stress-strain relationship of stainless steel under uniaxial stress state

In this paper, the Rasmussen's model [36] was chosen to describe the stress-strain behaviour of stainless steel, as presented in Eq. A.1.1.

$$\varepsilon=\begin{cases}\dfrac{\sigma}{E_0}+0.002\left(\dfrac{\sigma}{\sigma_{0.2}}\right)^{n} & \sigma\le\sigma_{0.2}\\ \dfrac{\sigma-\sigma_{0.2}}{E_{0.2}}+\varepsilon_{\mathrm{u}}\left(\dfrac{\sigma-\sigma_{0.2}}{\sigma_{\mathrm{u}}-\sigma_{0.2}}\right)^{m}+\varepsilon_{0.2} & \sigma>\sigma_{0.2}\end{cases} \quad \text{A.1.1}$$

in which the strain-hardening exponents n and m, the tangent modulus $E_{0.2}$ at nominal yield stress, the ultimate stress σ_{u} and corresponding strain ε_{u} can be calculated using Eqs. A.1.2-A.1.8.

$$n=\frac{ln\,20}{ln\,(\sigma_{0.2}/\sigma_{0.01})} \quad \text{A.1.2}$$

$$E_{0.2}=\frac{E_0}{1+0.002n/e} \quad \text{A.1.3}$$

$$e=\frac{\sigma_{0.2}}{E_0} \quad \text{A.1.4}$$

$$\frac{\sigma_{0.2}}{\sigma_{\mathrm{u}}}=\frac{0.2+185e}{1-0.0375(n-5)} \quad \text{A.1.5}$$

$$\varepsilon_{\mathrm{u}}=1-\frac{\sigma_{0.2}}{\sigma_{\mathrm{u}}} \quad \text{A.1.6}$$

$$m=1+3.5\frac{\sigma_{0.2}}{\sigma_{\mathrm{u}}} \quad \text{A.1.7}$$

$$\varepsilon_{0.2}=\frac{\sigma_{0.2}}{E_0}+0.002 \quad \text{A.1.8}$$

A.2. Stress-strain relationship of stainless steel under biaxial stress state

According to incremental theory, the stress-strain relationships of stainless steel under biaxial stress state are described as follows:

A.2.1 Elastic stage: $\sigma_{\mathrm{s}}\le f_{\mathrm{p}}$

$$\begin{bmatrix}\sigma_{\mathrm{s,c}}\\ \sigma_{\mathrm{s,v}}\end{bmatrix}=\frac{E_0}{1-\mu_{\mathrm{s}}^2}\begin{bmatrix}1 & \mu_{\mathrm{s}}\\ \mu_{\mathrm{s}} & 1\end{bmatrix}\begin{bmatrix}\varepsilon_{\mathrm{s,c}}\\ \varepsilon_{\mathrm{s,v}}\end{bmatrix} \quad \text{A.2.1}$$

Compared with carbon steel, the proportional limit f_{p} of stainless steel is primarily in

the range of 30-60% of nominal yield stress [43]. Therefore, the value of $f_p/\sigma_{0.2}$ is taken as 0.35, as suggested by Guo et al. [17].

$$f_p=0.35\sigma_{0.2} \quad \text{A.2.2}$$

A.2.2 Elastic-plastic stage: $f_p<\sigma_s\leq\sigma_{0.2}$

$$\begin{bmatrix}d\sigma_{s,c}\\ d\sigma_{s,v}\end{bmatrix}=\frac{E_s^t}{1-\mu_{sp}^2}\begin{bmatrix}1 & \mu_{sp}\\ \mu_{sp} & 1\end{bmatrix}\begin{bmatrix}d\varepsilon_{s,c}\\ d\varepsilon_{s,v}\end{bmatrix} \quad \text{A.2.3}$$

$$\mu_{sp}=(0.45-\mu_s)\frac{\sigma_s-f_p}{\sigma_{0.2}-f_p}+\mu_s \quad \text{A.2.4}$$

$$E_s^t=\frac{(\sigma_{0.2}-\sigma_s)\sigma_s}{(\sigma_{0.2}-f_p)f_p}(E_0-E_{0.2})+E_{0.2} \quad \text{A.2.5}$$

$$\sigma_s=\sqrt{\sigma_{s,c}^2+\sigma_{s,v}^2-\sigma_{s,c}\sigma_{s,v}} \quad \text{A.2.6}$$

in which μ_{sp} is the Poisson's ratio during elastic-plastic phase, E_s^t is the tangent modulus of stainless steel, which declined from E_0 to $E_{0.2}$ and σ_s is equivalent stress.

A.2.3 Starin hardening stage: $\sigma_s>\sigma_{0.2}$

$$\begin{bmatrix}d\sigma_{s,c}\\ d\sigma_{s,v}\end{bmatrix}=\frac{E_0}{Q}\begin{bmatrix}\sigma_v'+2p & -\sigma_v'\sigma_c'+2\mu_s p\\ -\sigma_v'\sigma_c'+2\mu_s p & \sigma_v'+2p\end{bmatrix}\begin{bmatrix}d\varepsilon_{s,c}\\ d\varepsilon_{s,v}\end{bmatrix} \quad \text{A.2.7}$$

$$\sigma_v'=\sigma_{s,v}-\sigma_m \quad \text{A.2.8}$$

$$\sigma_c'=\sigma_{s,c}-\sigma_m \quad \text{A.2.9}$$

$$\sigma_m=(\sigma_{s,v}+\sigma_{s,c})/3 \quad \text{A.2.10}$$

$$p=\frac{2H'}{9E_0}\sigma^2 \quad \text{A.2.11}$$

$$H'=\frac{d\sigma}{d\varepsilon_p}=10^{-3}E_0^2 \quad \text{A.2.12}$$

$$Q=\sigma_c'^2+\sigma_v'^2+2\mu_s\sigma_c'\sigma_v'+2H'(1-\mu_s)\sigma_s{}^2/9G \quad \text{A.2.13}$$

$$G=\frac{E_0}{2(1+\mu_s)} \quad \text{A.2.14}$$

where σ_v' and σ_c' are deviatoric stresses in vertical and circumferential directions, respectively, σ_m is the mean stress, G refers to the shear modulus.

Appendix B. Comparisons between test curves and proposed vertical stress-strain relationships of RAC-FSSTs

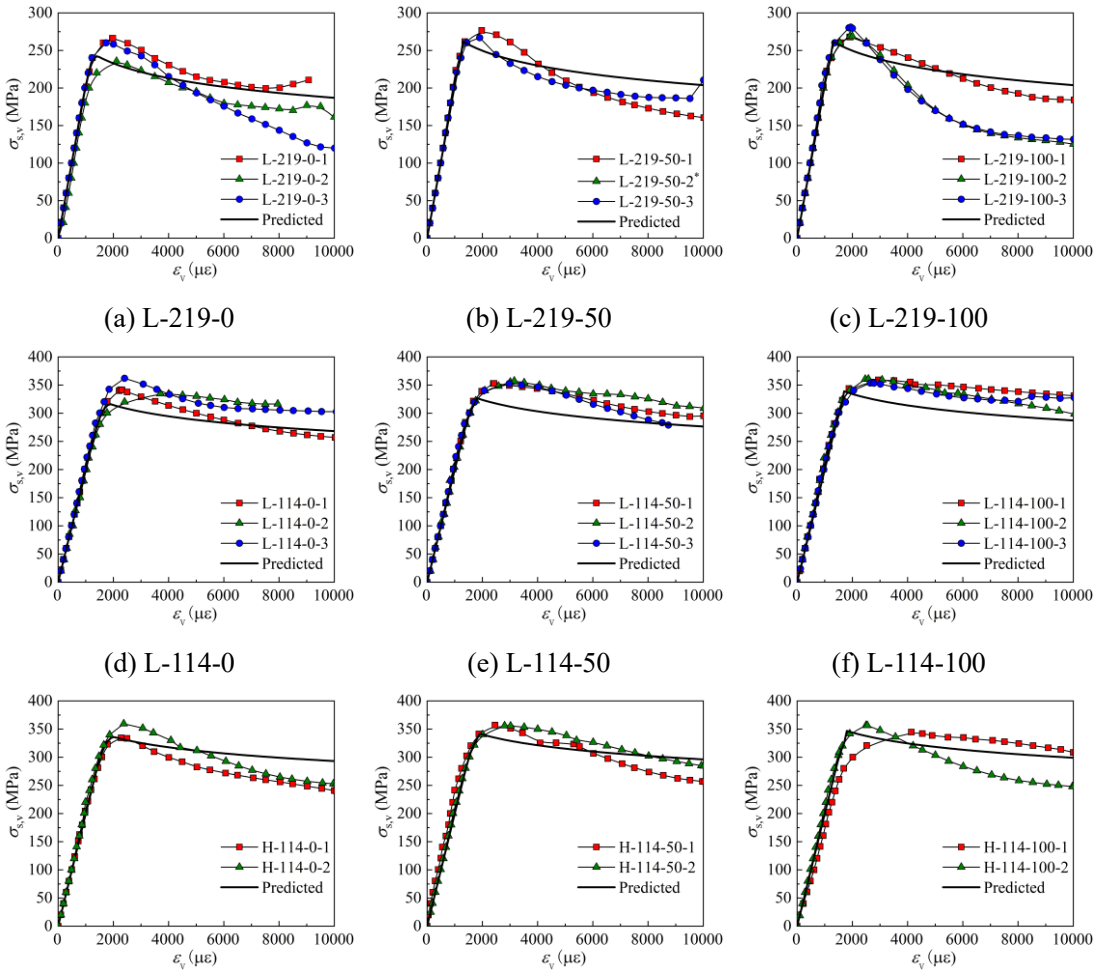

(a) L-219-0 (b) L-219-50 (c) L-219-100

(d) L-114-0 (e) L-114-50 (f) L-114-100

(g) H-114-0 (h) H-114-50 (i) H-114-100

Fig. B.1. Comparisons between test curves and $\sigma_{s,v}$-ε_v relationships of external steel tube.

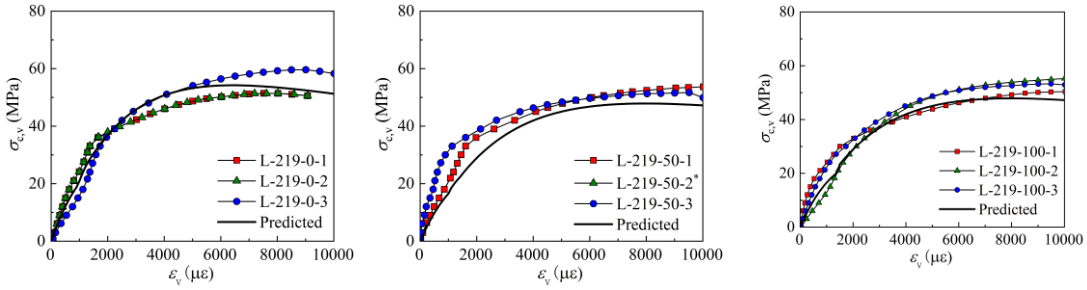

(a) L-219-0 (b) L-219-50 (c) L-219-100

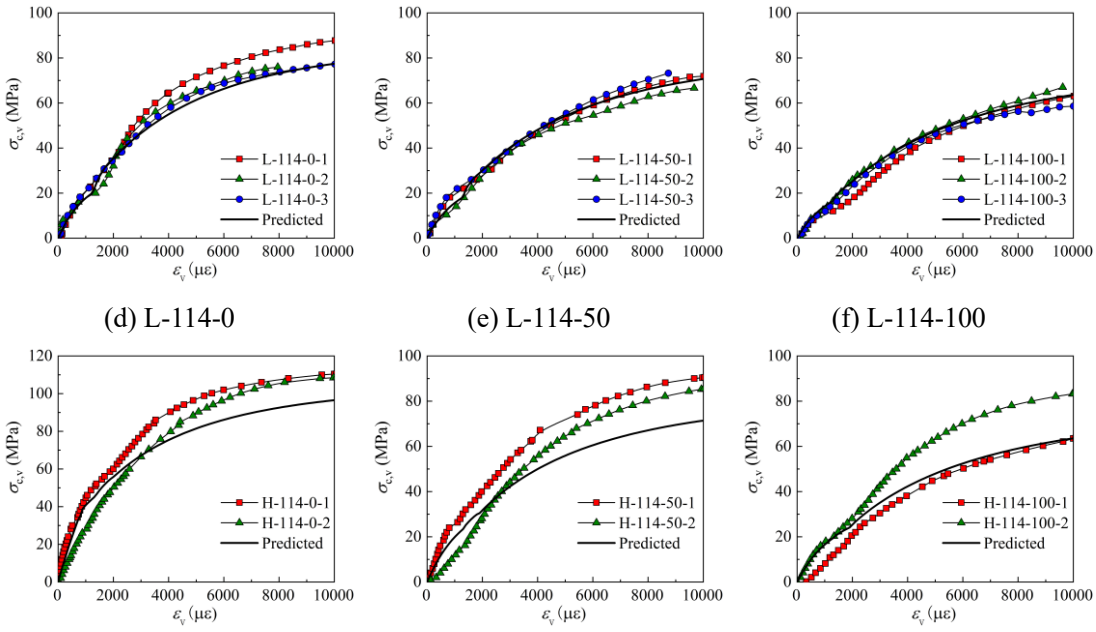

(d) L-114-0 (e) L-114-50 (f) L-114-100

(g) H-114-0 (h) H-114-50 (i) H-114-100

Fig. B.2. Comparisons between test curves and $\sigma_{c,v}$-ε_v relationships of core RAC.

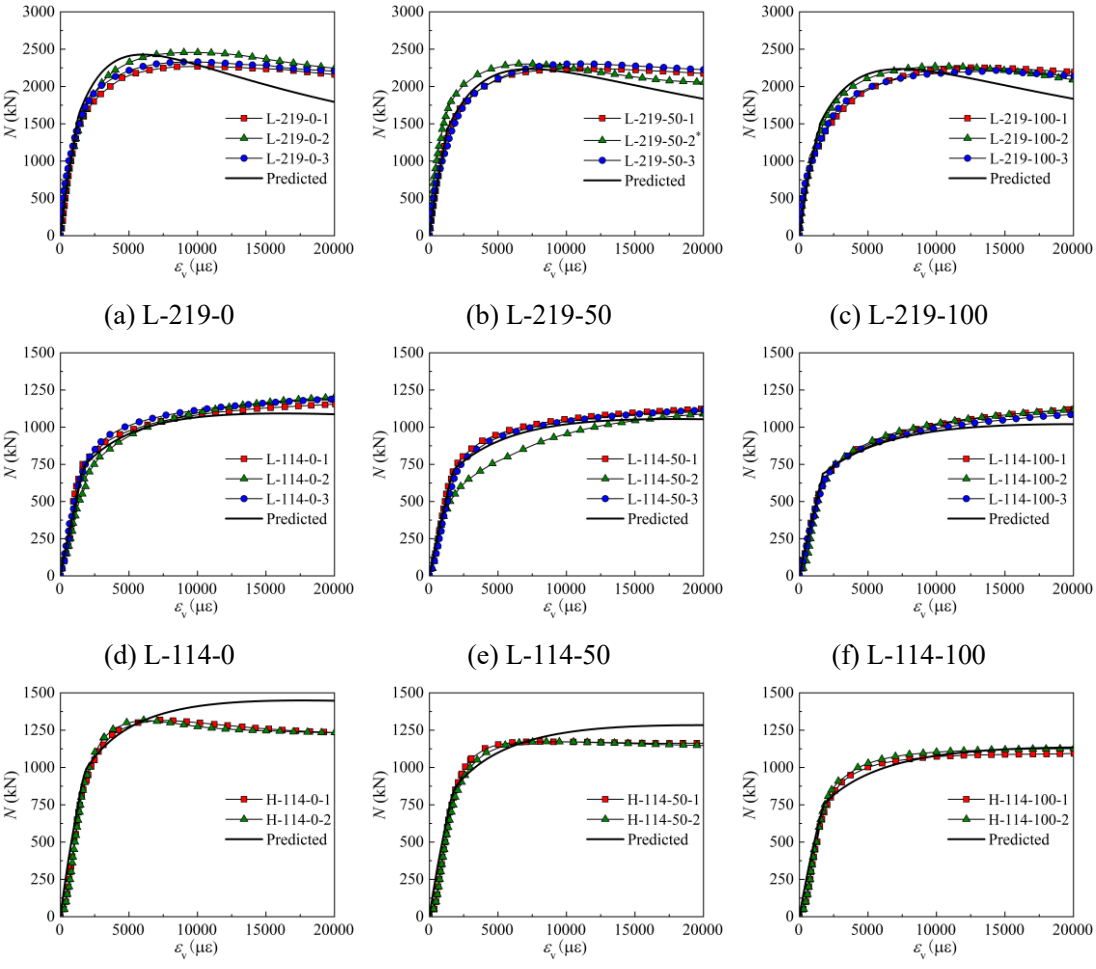

(a) L-219-0 (b) L-219-50 (c) L-219-100

(d) L-114-0 (e) L-114-50 (f) L-114-100

(g) H-114-0 (h) H-114-50 (i) H-114-100

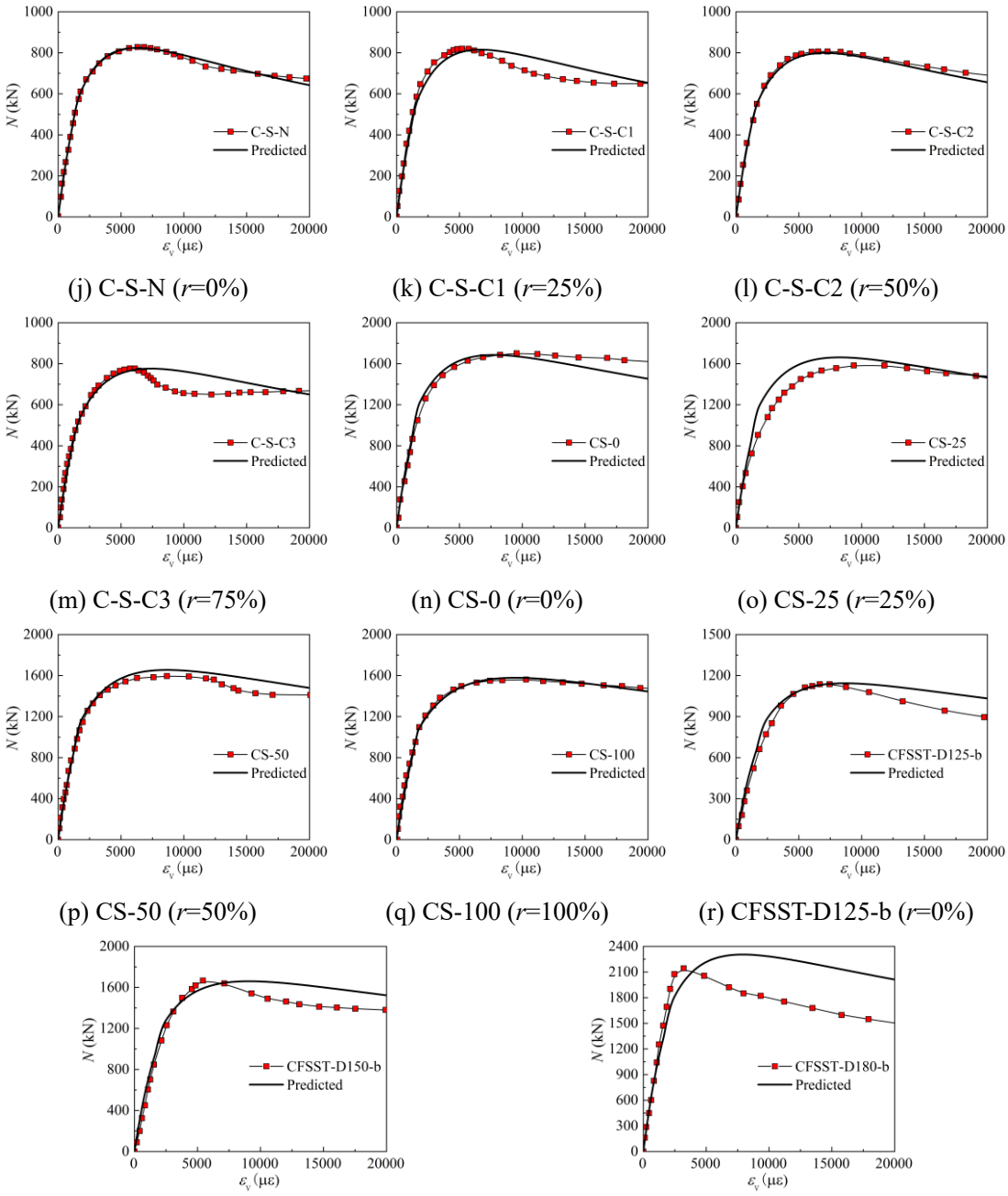

(j) C-S-N (*r*=0%) (k) C-S-C1 (*r*=25%) (l) C-S-C2 (*r*=50%)

(m) C-S-C3 (*r*=75%) (n) CS-0 (*r*=0%) (o) CS-25 (*r*=25%)

(p) CS-50 (*r*=50%) (q) CS-100 (*r*=100%) (r) CFSST-D125-b (*r*=0%)

(s) CFSST-D150-b (*r*=0%) (t) CFSST-D180-b (*r*=0%)

Fig.B.3. Comparisons between test curves and N-ε_v models of RAC-FSSTs and CFSSTs: (a)-(i) from this study; (j)-(m) from Yang and Ma [11]; (n)-(q) from Tam et al. [18]; (r)-(t) from Guo et al. [17].

References

[1] B. Young, E. Ellobody, Experimental investigation of concrete-filled cold-formed high strength stainless steel tube columns, J. Constr. Steel Res. 62 (2006) 484-492.

[2] L.H. Han, F. Chen, F.Y. Liao, Z. Tao, B. Uy, Fire performance of concrete filled stainless steel tubular columns, Eng. Struct. 56 (2013) 165-181.

[3] L.H. Han, C.Y. Xu, Z. Tao, Performance of concrete filled stainless steel tubular (CFSST) columns and joints: Summary of recent research, J. Constr. Steel Res. 152 (2019) 117-131.

[4] H. Zhao, R. Wang, C.C. Hou, D. Lam, Performance of circular CFDST members with external stainless steel tube under transverse impact loading, Thin-Walled Struct. 145 (2019) 106380.

[5] H. Zhao, R. Wang, D. Lam, C.C. Hou, R. Zhang, Behaviours of circular CFDST with stainless steel external tube: Slender columns and beams, Thin-Walled Struct. 158 (2021) 107172.

[6] Z. Chen, J. Xu, J. Xue, Y. Su, Performance and calculations of recycled aggregate concrete-filled steel tubular (RACFST) short columns under axial compression, Int J Steel Struct. 14 (2014) 31-42.

[7] Y. Geng, Y.Y. Wang, J. Chen, Time-dependent behaviour of steel tubular columns filled with recycled coarse aggregate concrete, J. Constr. Steel Res. 122 (2016) 455-468.

[8] Y.Y. Wang, Y. Geng, Y. Chang, C. Zhou, Time-dependent behaviour of recycled concrete filled steel tubes using RCA from different parent waste material, Constr. Build. Mater. 193 (2018) 230-243.

[9] W.Q. Lyu, L.H. Han, Investigation on bond strength between recycled aggregate concrete (RAC) and steel tube in RAC-filled steel tubes, J. Constr. Steel Res. 155 (2019) 438-459.

[10] A. He, A. Su, Y. Liang, O. Zhao, Experimental and numerical investigations of circular recycled aggregate concrete-filled stainless steel tube columns, J. Constr. Steel Res. 179 (2021) 106566.

[11] Y.F. Yang, G.L. Ma, Experimental behaviour of recycled aggregate concrete filled stainless steel tube stub columns and beams, Thin-Walled Struct. 66 (2013) 62-75.

[12] Y.Y. Wang, J. Chen, Y. Geng, Testing and analysis of axially loaded normal-strength recycled aggregate concrete filled steel tubular stub columns, Eng. Struct. 86 (2015) 192-212.

[13] M.Z. Zhao, Y.Y. Wang, D.E. Lehman, Y. Geng, C.W. Roeder, Response and modeling of axially-loaded concrete-filled steel columns with recycled coarse and fine aggregate, Eng. Struct. 234 (2021) 111733.

[14] W.Q. Lyu, L.H. Han, C. Hou, Axial compressive behaviour and design calculations on recycled aggregate concrete-filled steel tubular (RAC-FST) stub columns, Eng. Struct. 241 (2021) 112452.

[15] D. Lam, L. Gardner, Structural design of stainless steel concrete filled columns, J. Constr. Steel Res. 64 (2008) 1275-1282.

[16] B. Uy, Z. Tao, L.H. Han, Behaviour of short and slender concrete-filled stainless steel tubular columns, J. Constr. Steel Res. 67 (2011) 360-378.

[17] L.H. Guo, Y. Liu, F. Fu, H.J. Huang, Behavior of axially loaded circular stainless steel tube confined concrete stub columns, Thin-Walled Struct. 139 (2019) 66-76.

[18] V.W.Y. Tam, Z.B. Wang, Z. Tao, Behaviour of recycled aggregate concrete filled stainless steel stub columns, Mater. Struct. 47 (2014) 293-310.

[19] BS EN 1994-1-1: 2004, Design of Composite Steel and Concrete Structures, Part1.1, General Rules and Rules for Building, British Standards Institution, London, 2004.

[20] Architectural Institute of Japan. AIJ 2008: recommendations for design and construction of concrete filled steel tubular structures. Tokyo: AIJ; 2008.

[21] GB 50936-2014, Technical code for concrete filled steel tubular structures, China Architecture & Building Press, Beijing, China, 2014.

[22] ANSI/AISC 360-16, Specification for Structural Steel Buildings, American Institute of Steel Construction, Chicago, 2016.

[23] T/CECS 625-2019, Technical specification for recycled aggregate concrete-filled steel tubular structures, China Architecture & Building Press, Beijing, China, 2020.

[24] EN ISO 6892-1, Metallic Materials - Tensile Testing - Part 1: Method of Test at Room Temperature, European Committee for Standardization (CEN), Brussels, 2009.

[25] H. Zhao, F.Q. Liu, H. Yang, Thermal properties of coarse RCA concrete at elevated temperatures, Appl. Therm. Eng. 140 (2018) 180-189.

[26] H. Zhao, F.Q. Liu, H. Yang, Residual compressive response of concrete produced with both coarse and fine recycled concrete aggregates after thermal exposure, Constr. Build. Mater. 244 (2020) 118397.

[27] Z. Tao, B. Uy, F.Y. Liao, L.H. Han, Nonlinear analysis of concrete-filled square stainless steel stub columns under axial compression, J. Constr. Steel Res. 67 (2011) 1719-1732.

[28] Y.L. Li, X.L. Zhao, R.K. Singh Raman, Theoretical model for concrete-filled stainless steel circular stub columns under axial compression, J. Constr. Steel Res. 157 (2019) 426-439.

[29] Z.B. Wang, Z. Tao, L.H. Han, B. Uy, D. Lam, W.H. Kang, Strength, stiffness and ductility of concretefilled steel columns under axial compression, Eng. Struct. 135 (2017) 209-221.

[30] Y.F. Yang, L.H. Han, Compressive and flexural behaviour of recycled aggregate concrete filled steel tubes (RACFST) under short-term loadings, Steel. Compos. Struct. 6 (2006) 257-284.

[31] J. Chen, Y.Y. Wang, C.W. Roeder, J. Ma, Behavior of normal-strength recycled aggregate concrete filled steel tubes under combined loading, Eng. Struct.130 (2017) 23-40.

[32] P. Chen, Y.Y. Wang, C.Y. Liu, Confinement path-dependent analytical model for FRP-confined concrete and concrete-filled steel tube subjected to axial compression, Compos. Struct. 201 (2018) 234-247.

[33] J. Chen, S.M. Zhang, Y.Y. Wang, Y. Geng, Axial compressive behavior of recycled concrete filled steel tubular stub columns with the inclusion of crushed brick, Struct. 26 (2020) 271-283.

[34] Y.Y. Wang, Y. Geng, G. Ranzi, S.M. Zhang, Time-dependent behaviour of expansive concrete-filled steel tubular columns, J Constr Steel Res. 67 (2011) 471-483.

[35] Y. Geng, Y.Y. Wang, J. Chen, M.Z. Zhao, Time-dependent behaviour of 100% recycled coarse aggregate concrete filled steel tubes subjected to high sustained load level, Eng. Struct. 210 (2020) 110353.

[36] K.J.R. Rasmussen, Full-range stress-strain curves for stainless steel alloys, J Constr. Steel Res. 59 (2003) 47-61.

[37] M.H. Lai, J.C.M. Ho, A theoretical axial stress-strain model for circular concrete-filled-steel-tube columns, Eng. Struct. 125 (2016) 124-143.

[38] M.H. Lai, W. Song, X.L. Ou, M.T. Chen, Q. Wang, J.C.M. Ho, A path dependent stress-strain model for concrete-filled-steel-tube column, Eng. Struct. 211 (2020) 110312.

[39] J.C.M. Ho, X.L. Ou, C.W. Li, W. Song, Q. Wang, M.H. Lai, Uni-axial behaviour of expansive CFST and DSCFST stub columns, Eng. Struct. 237 (2021) 112193.

[40] J.B. Mander, M.J.N. Priestley, R. Park, Theoretical stress-strain model for confined concrete, J. Struct. Eng. 114 (1988) 1804-1826.

[41] G.F. Belén, M.A. Ferrnando, C.L. Diego, S.P. Sindy, Stress–strain relationship in axial compression for concrete using recycled saturated coarse aggregate. Constr. Build. Mater. 25 (2011) 2335-2342.

[42] S.P.C. Marques, D.C.D.S.C. Marques, J.L.D. Silva, M.A.A. Cavalcante, Model for analysis of short columns of concrete confined fiber-reinforced polymer. J. Compos. Constr. 8 (2004) 332-340.

[43] B. Young, W.M. Lui, Behavior of cold-formed high strength stainless steel sections. J. Struct. Eng. 131 (2005) 1738-1745.